Impact of Axial Shape Annealing Function Formulation on Three-Dimensional Core Power Reconstruction Using Ex-Core Detectors

*Minhyeok Bang, Junwoo Lee, and Yonghee Kim**
Korea Advanced Institute of Science and Technology
291, Daehak-ro, Yuseong-gu, Daejeon, Republic of Korea, 34141
mh_bang@kaist.ac.kr; junwoolee@kaist.ac.kr; yongheekim@kaist.ac.kr

Keywords : Proper orthogonal decomposition (POD), artificial neural networks, small modular reactors (SMR), ex-core neutron detectors, core-exit thermocouples (CET)

1. Introduction

Accurate monitoring of three-dimensional core power distributions is essential for reactor safety. However, reliance on in-core instrumentation such as self-powered neutron detectors increases system complexity and may reduce the economic competitiveness of small modular reactors. This study reconstructs three-dimensional core power distributions using only ex-core neutron detector signals and core-exit thermocouple (CET) data, without in-core measurements. Building on prior neural network–based [1] and POD-based approaches [2], the present work adopts a hybrid framework that combines physics-based decomposition with data-driven modelling.

The proposed approach employs proper orthogonal decomposition to represent the three-dimensional core power distribution of the ATOM [3] reactor in a reduced modal space, while an artificial neural network predicts the corresponding modal coefficients from ex-core detector and core-exit temperature signals.

In simulating ex-core detector responses, radial weighting factors and shape annealing functions are applied to the three-dimensional power distribution. In our previous implementations, it has been implicitly assumed that the axial shape annealing function (SAF) corresponding to the hot full power condition is sufficient for all operating states.

The primary objective of this study is to examine the validity of this assumption. Reconstruction performance obtained using a fixed hot full power–based shape annealing function is compared with that obtained using a power-dependent formulation to evaluate the impact of this assumption on reconstruction accuracy.

2. Methodologies

2.1 Simulation of Ex-core Detector and CET

In this study, the SAF treatment differs from our previous implementation. Instead of uniformly applying the hot full power–based SAF, the axial shape is linearly interpolated between the hot zero power and hot full power limiting shapes proposed by Roh et al. [4] according to reactor power level, as shown in Fig. 1.

Although originally developed for the SMART-660 core, the formulation in [4] is directly applicable here because the ATOM core shares identical core dimensions and assembly layout; thus, the same axial shape functions are used without modification. The radial weighting factors (RWFs) are likewise adopted from [4], and their spatial distributions are presented in Fig. 2, together with the checkerboard arrangement of the CET locations. Each CET signal is assumed proportional to the axially integrated linear power of the corresponding fuel assembly. Four slightly asymmetric ex-core detectors with three axial levels provide 12 signals, combined with 32 core-exit thermocouple signals, resulting in 44 input parameters.

This study aims to compare two SAF treatments. To assess the sensitivity of the proposed model to minute changes in two SAF configurations, we conducted a parallel analysis. The maximum RMS difference between the two ex-core signal values, calculated from either fixed-SAF or variable-SAF, was approximately 0.79%.

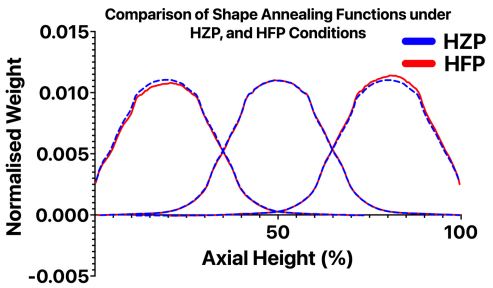

Fig. 1. Comparison of Shape Annealing Functions under HZP and HFP Conditions.

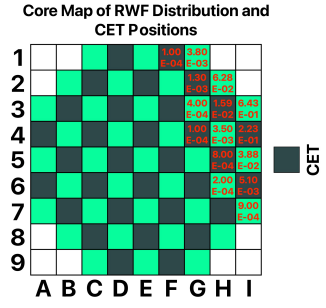

Fig. 2. Core Map of RWF Distribution and CET Locations.

2.2 Training Dataset Generation

The training data were generated using the in-house nodal PWR simulation code KANT [5] for the ATOM [3] small modular reactor, which consists of 69 fuel assemblies.
Figures 3–5 present the transient core power and axial shape index (ASI) profiles for Datasets A, B, and C, respectively.

Dataset A represents a normal load-follow operation with a 100–50–20% power sequence and contains 2,271 samples. Dataset B corresponds to the most challenging scenario, in which the centrally located control rod—undetectable by ex-core detectors—is fixed fully inserted, whilst the remaining rods are randomly manipulated, yielding 2,442 samples. Dataset C includes abnormal power distributions induced by random manipulation of all control rods and consists of 1,990 samples.

For each dataset, 80% of the samples were randomly assigned to the training set and the remaining 20% to the validation set. The final training dataset was constructed by combining the training subsets of Datasets A, B, and C, whilst validation for untrained data was performed separately using the remaining portions of each dataset.

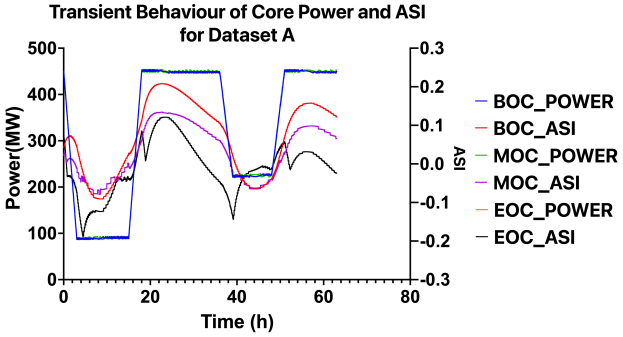

Fig. 3. Transient Core Power and Axial Shape Index (ASI) Responses for Dataset A.

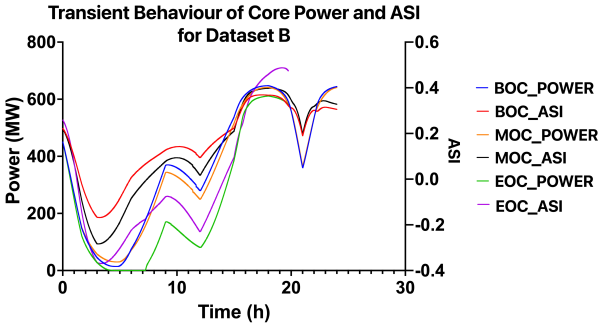

Fig. 4. Transient Core Power and Axial Shape Index (ASI) Responses for Dataset B.

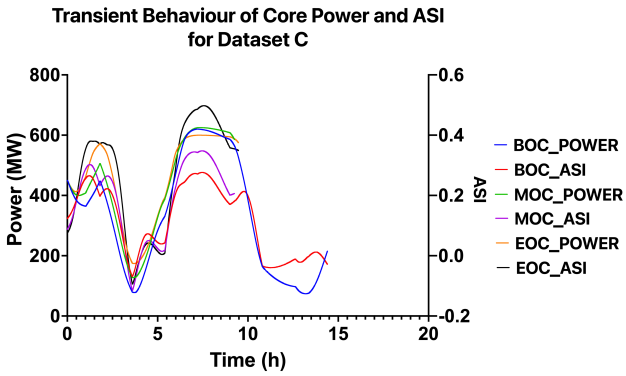

Fig. 5. Transient Core Power and Axial Shape Index (ASI) Responses for Dataset C.

2.3 POD-Based Representation of Core Power Distribution

Proper orthogonal decomposition (POD) is applied to the training dataset to obtain a low-dimensional representation of the three-dimensional core power distribution.

Let $A \in \mathbb{R}^{N\times M}$ denote a data matrix whose columns correspond to vectorised power distributions from M operating scenarios. After subtracting the mean distribution $\bar{a}$, the deviation matrix is defined as in (1),

$$A' = A - \bar{a}I^{\top} \tag{1}$$

Applying SVD to A′, in (2),

$$A' = U\Sigma V^{\top}, \tag{2}$$

yields orthonormal singular modes in U and corresponding modal coefficients in $\Sigma V^{\top}$, ordered by decreasing variance contribution. By retaining the first r dominant modes, the power distribution is represented in a low-rank subspace, reducing the effective degrees of freedom of the inverse problem. Accordingly, the three-dimensional power distribution for a single operating condition is approximated as shown in (3),

$$a \approx \bar{a} + U_r c, \tag{3}$$

where U_r is the truncated POD basis and $c \in \mathbb{R}^r$ is the reduced coefficient vector. For each operating condition, the reduced coefficient vector is obtained from the corresponding column of $\Sigma_r V_r^{\top}$. In this study, these reduced POD coefficients are treated as the prediction target. The mapping from ex-core detector signals and CET data to the POD coefficients is inherently nonlinear due to neutron transport and thermal–neutronic feedback. Therefore, a non-linear neural network model is employed to infer the POD coefficients, whilst the POD basis is kept fixed. The full power distribution is subsequently reconstructed using the predicted coefficients and the POD basis.

2.4 ANN Model Structures

A multilayer perceptron (MLP) was employed to infer the POD coefficients from the detector and CET signals. The network comprises three hidden layers with LeakyReLU activation (negative slope 0.2) and dropout regularisation (dropout rate 0.3).

Multiple model versions were constructed by varying the number of retained POD basis modes, whilst keeping the overall network architecture identical. Sixteen model configurations were initially developed, and seven representative models (M30, M44, M50, M96, M128, M192, and M256) are presented in this paper. The purpose of considering multiple modal truncation levels is not to propose an optimal architecture, but to ensure that the comparison between fixed and variable SAF formulations is not biased by a particular choice of modal dimension.

The corresponding network configurations and retained POD modes are summarised in Table 1.

Table I: MLP models' specifications

Version	1st layer	2nd layer	3rd layer	SVD modes
M256	256	1024	4096	256
M192	256	1024	4096	192
M128	256	1024	4096	128
M96	256	1024	4096	96
M50	256	1024	4096	50
M44	256	1024	4096	44
M30	256	1024	4096	30

3. Numerical Results

3.1 Models' Training Performance

Figures 6 and 7 present the training histories on the training dataset, where the mean reconstruction RMSE as a function of epoch is used as the primary indicator of convergence behaviour. A comparison of the final RMSE values indicates that the optimal model depends on the SAF treatment. Under the fixed-SAF assumption, M128 achieves the lowest final RMSE, whereas M50 yields the smallest RMSE when the variable-SAF formulation is applied.

This tendency is also reflected in Tables II and III. In the fixed-SAF case, M128 exhibits the lowest mean RMSE, which is consistent with the trend observed in Fig. 6, whilst the smallest maximum RMSE is obtained with M192. In contrast, for the variable-SAF formulation, M50 achieves both the lowest mean RMSE and the lowest maximum RMSE, which agrees with the convergence behaviour shown in Fig. 7.

Adopting the variable SAF generally reduces the maximum RMSE for models with fewer SVD modes from M128 to M30. However, it increased the maximum RMSE for M192, and the overall differences remain marginal.

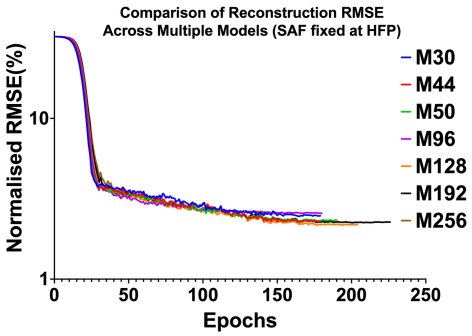

Fig. 6. Training convergence of models with SAF fixed at HFP.

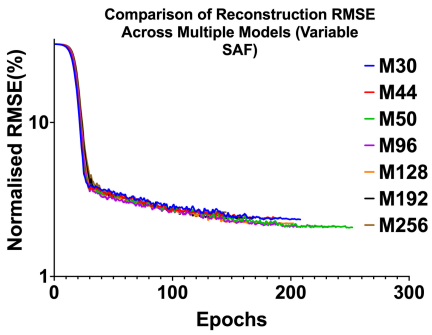

Fig. 7. Training convergence of models with variable SAF between HZP and HFP.

Table II: Whole-core reconstruction normalised RMSE on Training Dataset (SAF fixed at HFP)

Version	Mean	Max	Min
M256	2.56%	9.56%	0.77%
M192	2.20%	8.02%	0.71%
M128	**2.15%**	**9.40%**	**0.65%**
M96	2.52%	9.24%	0.75%
M50	2.24%	9.04%	0.77%
M44	2.26%	9.64%	0.68%
M30	2.45%	9.86%	0.74%

Table III: Whole-core reconstruction normalised RMSE on Training Dataset (Variable SAF)

Version	Mean	Max	Min
M256	2.57%	9.54%	0.77%
M192	2.30%	8.15%	0.75%
M128	2.16%	8.68%	0.64%
M96	2.07%	8.66%	0.62%
M50	**2.04%**	**8.09%**	**0.60%**
M44	2.32%	8.24%	0.81%
M30	2.31%	8.60%	0.67%

3.2 Validation on Untrained Datasets

The validation results on the unseen Dataset C, which exhibits the highest reconstruction errors among the tested datasets, are summarised in Tables IV–VII. In this study, the best-performing model is identified based on two criteria: the maximum whole-core reconstruction

RMSE and the maximum absolute peak power relative error. No consistent ranking is observed across the tested model versions, and different metrics identify different best-performing configurations, indicating the absence of a dominant architecture under unseen conditions.

Table IV and Table V reveal a reduction in the maximum whole-core RMSE for M30, M44, M50, M96, M192 and M256 using the variable SAF formulation. However, the reduction in error remains relatively small and lacks systematic gain. This ultimately results in an increase in error for M128.

Table IV: Whole-core reconstruction normalised RMSE on Dataset C (Fixed SAF)

Version	Mean	Max	Min
M256	2.84%	6.72%	1.65%
M192	2.30%	5.57%	1.26%
M128	**2.23%**	**5.25%**	**1.21%**
M96	2.65%	5.58%	1.38%
M50	2.34%	5.69%	1.17%
M44	2.43%	6.63%	1.14%
M30	2.65%	6.14%	1.27%

Table V: Whole-core reconstruction normalised RMSE on Dataset C (Variable SAF)

Version	Mean	Max	Min
M256	2.82%	6.65%	1.67%
M192	2.42%	5.50%	1.41%
M128	2.24%	5.34%	1.22%
M96	**2.14%**	**4.95%**	**1.20%**
M50	2.13%	5.19%	1.13%
M44	2.43%	5.69%	1.19%
M30	2.44%	4.97%	1.29%

A similar trend is also observed in the peak power absolute error statistics. As shown in Tables VI and VII, M30, M50, M96, M128 have seen a reduction in maximum peak power error when the variable SAF was applied, whilst for M44, M192, M256, the errors have increased. This suggests that there is no clear trend of performance gain or decrease over the different SAF models. Also note that even though only M96 showed non-zero minimum peak power error in Table VI, this is caused by truncation and doesn't imply a significant difference in performance.

Table VI: Absolute peak power relative error on Dataset C (Fixed SAF)

Version	Mean	Max	Min
M256	0.83%	6.30%	0.00%
M192	0.75%	4.75%	0.00%
M128	0.78%	4.84%	0.00%
M96	0.83%	5.58%	0.04%
M50	0.76%	4.59%	0.00%
M44	**0.79%**	**4.24%**	**0.00%**
M30	0.89%	4.73%	0.00%

Table VII: Absolute peak power relative error on Dataset C (Variable SAF)

Version	Mean	Max	Min
M256	0.81%	6.31%	0.00%
M192	0.76%	5.00%	0.00%
M128	0.71%	4.60%	0.00%
M96	0.69%	4.53%	0.00%
M50	0.67%	4.49%	0.00%
M44	0.75%	4.33%	0.00%
M30	**0.76%**	**4.26%**	**0.00%**

3. Conclusions

The proposed POD–ANN framework demonstrated feasible reconstruction using just ex-core detector and CET signals. Overall, it showed acceptable power distribution estimation with a simplified ex-core detector response function. Reconstruction accuracy wasn't strongly affected by the SAF formulation.

Within the tested datasets and configurations, replacing fixed HFP-based SAF with a power-dependent SAF didn't consistently improve performance. So, the fixed HFP-based SAF might be a reasonable simplification for this framework, though some model/dataset combinations benefited from the variable SAF.

This suggests that the current model's power distribution prediction resolution isn't sufficiently high to detect such a subtle power dependence in SAF formulation.

ACKNOWLEDGEMENT

This work was supported by the Innovative Small Modular Reactor Development Agency grant funded by the Korea Government (MIST/MCEE) (No. RS-2024-00405419) and by the Korea Energy Technology Evaluation and Planning (KETEP) grant funded by the Korean Government (MTIE) (No. RS-2024-00439210).

REFERENCES

[1] Li W. et al., Core power distribution reconstruction using artificial neural networks, *Nucl. Eng. Technol.*, 54 (2022) 617–626.
[2] Urase Y. et al., POD-based in-core power distribution reconstruction using ex-core detectors for HTGRs, *J. Nucl. Sci. Technol.*, 2025.
[3] Jeong Y. et al., Load-follow operation capability of soluble boron-free SMR ATOM, *Front. Energy Res.*, 13 (2025) 1639569.
[4] Roh G. et al., Ex-core detector response evaluation of the SMART reactor using DORT, *J. Nucl. Sci. Technol.*, 45 (2008) 78–81.
[5] Oh T. et al., Development and validation of the multiphysics PWR core simulator KANT, *Nucl. Eng. Technol.*, 55 (2023) 2230–2245.